Predictability of the Seasonal Mean Atmospheric Circulation during Autumn, Winter, and Spring

DAVID STRAUS AND J. SHUKLA

George Mason University, Fairfax, Virginia, and Center for Ocean–Land–Atmosphere Studies, Calverton, Maryland

DAN PAOLINO

Center for Ocean–Land–Atmosphere Studies, Calverton, Maryland

SIEGFRIED SCHUBERT, MAX SUAREZ, AND PHILIP PEGION*

NASA Goddard Space Flight Center, Greenbelt, Maryland

ARUN KUMAR

National Centers for Environmental Prediction, Washington, D.C.

(Manuscript received 12 September 2002, in final form 23 May 2003)

ABSTRACT

The predictability of the autumn, boreal winter, and spring seasons with foreknowledge of sea surface temperatures (SSTs) is studied using ensembles of seasonal simulations of three general circulation models (GCMs): the Center for Ocean–Land–Atmosphere Studies (COLA) GCM, the National Aeronautics and Space Administration Seasonal to Interannual Prediction Project (NSIPP) GCM, and the National Centers for Environmental Prediction (NCEP) GCM. Warm-minus-cold composites of the ensemble mean and observed tropical Pacific precipitation, averaged for the three warmest El Niño and three coldest La Niña winters, show large positive anomalies near the date line that extend eastward to the South American coast. The same is true for composites of the spring following the event. In the composites of the autumn preceding the event, the precipitation is weaker and shifted off the equator in the far eastern Pacific, where equatorial SSTs are too low to support convection. The corresponding boreal winter 200-hPa height composites show strong signals in the Tropics and midlatitudes of both hemispheres. The subsequent spring composites are similar, but weaker in the northern extratropics. In the preceding autumn composites, the overall height signal is quite weak, except in the southern Pacific.

The model dependence of the signal (variance of ensemble means) and noise (variance about the ensemble means) of the seasonal mean 200-hPa height is small, a result that holds for all three seasons and is in contrast to earlier studies. The signal-to-noise ratio is significantly greater than unity in the Tropics (all seasons), the northern Pacific and continental North America subtropics (boreal winter and spring), and the southern Pacific subtropics (boreal autumn).

Rotated empirical orthogonal function analysis of the tropical Pacific SST recovers El Niño–like dominant patterns in boreal winter and spring, but emphasizes two SST patterns in autumn, one with largest SST in the far eastern tropical Pacific and one with a maximum nearer the date line. Two methods are used to assess the precipitation and height field responses to these patterns: linear regression of the ensemble means on the principal component (PC) time series of SST and identification of patterns that optimize the signal-to-noise ratio. The two methods yield remarkably similar results.

The optimal height patterns for boreal winter and spring are similar, although the spring response over the northern extratropics is somewhat weaker, and some subtle changes in phase are found in all three GCMs. The associated optimal time series have serial correlations with the leading PC of SST that exceed 0.9 for all GCMs for winter and spring. For autumn the time series of the leading two optimal patterns each has a serial correlation with the corresponding PC of SST that exceeds 0.7 for the COLA and NSIPP GCMs. The autumn 200-hPa-height leading optimal pattern (response to eastern Pacific SST) is quite weak, representing nearly uniform tropical warming. The second optimal pattern (response to central Pacific SST) shows a robust wave train in the southern Pacific, with a consistent belt of low height over northern midlatitudes.

* Current affiliation: Science Applications International Corporation, Beltsville, Maryland.

Corresponding author address: David M. Straus, 4041 Powder Mill Rd., Ste. 302, Calverton, MD 20705.
E-mail: straus@cola.iges.org

1. Introduction

Boundary-forced predictability on the seasonal timescale depends in a direct way on the extent to which the boundary condition anomalies, primarily tropical sea surface temperature (SST), produce strong anomalous atmospheric heat and momentum sources. Enhanced predictability in midlatitudes is only realized if the remote circulation forced by these heat and momentum sources is strong enough and consistent enough to be distinguishable from the chaotic internal variability (sometimes called noise) of the midlatitude atmosphere. The presence of this internal variability can lead to substantial uncertainty in the expected seasonal mean even in the presence of large boundary anomalies.

The need to understand the characteristics of this variability, and to learn how to distinguish it from the response forced by the boundary, has motivated a great deal of recent general circulation model (GCM) based research (e.g., Straus and Shukla 2000, 2002; Schubert et al. 2001; Shukla et al. 2000a,b; Chang et al. 2000; Brankovic and Palmer 2000; Kumar et al. 2000). GCMs are particularly useful in this regard, since they can provide estimates of the signal and the noise via an ensemble of seasonal solutions generated with identical boundary conditions of SST, but with different initial conditions. The disadvantage of using GCMs is of course that the signal and noise estimates are likely to be model dependent and may not be accurate. Exploring this dependence is one of the goals of the Dynamical Seasonal Prediction (DSP) project (Shukla et al. 2000a), a multi-institutional cooperation aimed at better understanding seasonal predictability. [The July 2000 issue of the *Quarterly Journal of the Royal Meteorological Society*, Vol. 126B, No. 567, was devoted to the DSP project and its European equivalent, the Prediction of Climate Variations on Seasonal to Interannual Timescales (PROVOST) project.] Recently, other authors have also recognized the importance of exploring the model dependence of predictability estimates (e.g., Hoerling et al. 2001).

Traditionally, research on SST-forced seasonal predictability has focused on boreal winter, when the tropical Pacific SST anomalies associated with the El Niño–Southern Oscillation (ENSO) episodes are strong, the radiative forcing of the general circulation is nearly constant, and the response in the northern extratropics is well defined. Recent work on the response to ENSO during other times of the year has suggested that the early (boreal) spring response is distinguishable from the noise, but that during summer and autumn the signal is much weaker (Brankovic and Palmer 1997, 2000; Kumar and Hoerling 1998; Livezey et al. 1997). Schubert et al. (2002, hereafter S2) do show that during summer the concomitant reduction in noise leads to signal-to-noise ratios that are comparable to those found for winter.

The purpose of this paper is to systematically explore and compare characteristics of the SST-forced signal and the associated noise in boreal autumn, winter, and spring, utilizing ensemble simulations made with three GCMs. We compare the signal patterns that optimize the signal-to-noise ratio for the three GCMs and relate them to different patterns of tropical SST forcing. The optimal patterns depend on the complete set of ensemble simulations, not just the ensemble mean. The ability to assess these patterns is a second attraction of using GCM ensemble simulations. Comparison of these optimal patterns among GCMs for tropical SST forcing has not previously appeared in the literature.

TABLE 1. Summary of GCMs, showing horizontal resolution in triangular truncation for spectral models, latitude by longitude resolution for the gridpoint model, number of vertical levels *L*, and number of ensemble members *N*.

GCM	Resolution	*L*	*N*	Reference
COLA	T63	18	10	Schneider (2002)
NSIPP	2.0° × 2.5°	34	9	Bacmeister and Suarez (2002)
NCEP	T62	28	10	Kanamitsu et al. (2002)

This paper extends previous DSP intermodel comparison studies from the winter season to the transition seasons in a unified framework. Ensembles of seasonal simulations of the three GCMs we study (see Table 1) were generated for boreal spring (autumn) for the 18 yr from 1981 to 1998 (1982 to 1999), using the same observed SSTs (Reynolds and Smith 1994) and realistic initial conditions. In order to facilitate comparison of the transition season results with the boreal winter season, we have also run winter cases using the calendar years of 1981/82–1998/99 for the same three GCMs. (See section 2 for further details of the GCMs.) The winter results will help to put the transition seasons in context.

We find that in boreal spring, as in winter, large eastern tropical Pacific SST anomalies force a significant and realistic signal in the tropical Pacific and in both the northern and southern extratropics. The signal in boreal autumn is much weaker, however. In order to highlight the seasonal differences in a familiar context, we show time series of the pattern correlation of 200-hPa height between the ensemble (seasonal) mean anomaly of each GCM and the seasonal mean anomaly from observations (Fig. 1). The pattern correlation is taken over the Pacific–North America region (15°–70°N, 180°–60°W). The years are presented (from left to right) in order of increasing absolute value of the Niño-3 index,[1] with red (blue) indicating El Niño (La Niña) years. The three bars shown for each year indicate the result for the three GCMs (always in the same order). For the winter season (middle panel), both the strength and consistency of the GCM pattern correlations are strongly

[1] Niño-3 is defined as the SST anomaly averaged over the area 5°S–5°N, 150°–90°W, and is obtained from the data of Smith et al. (1996).

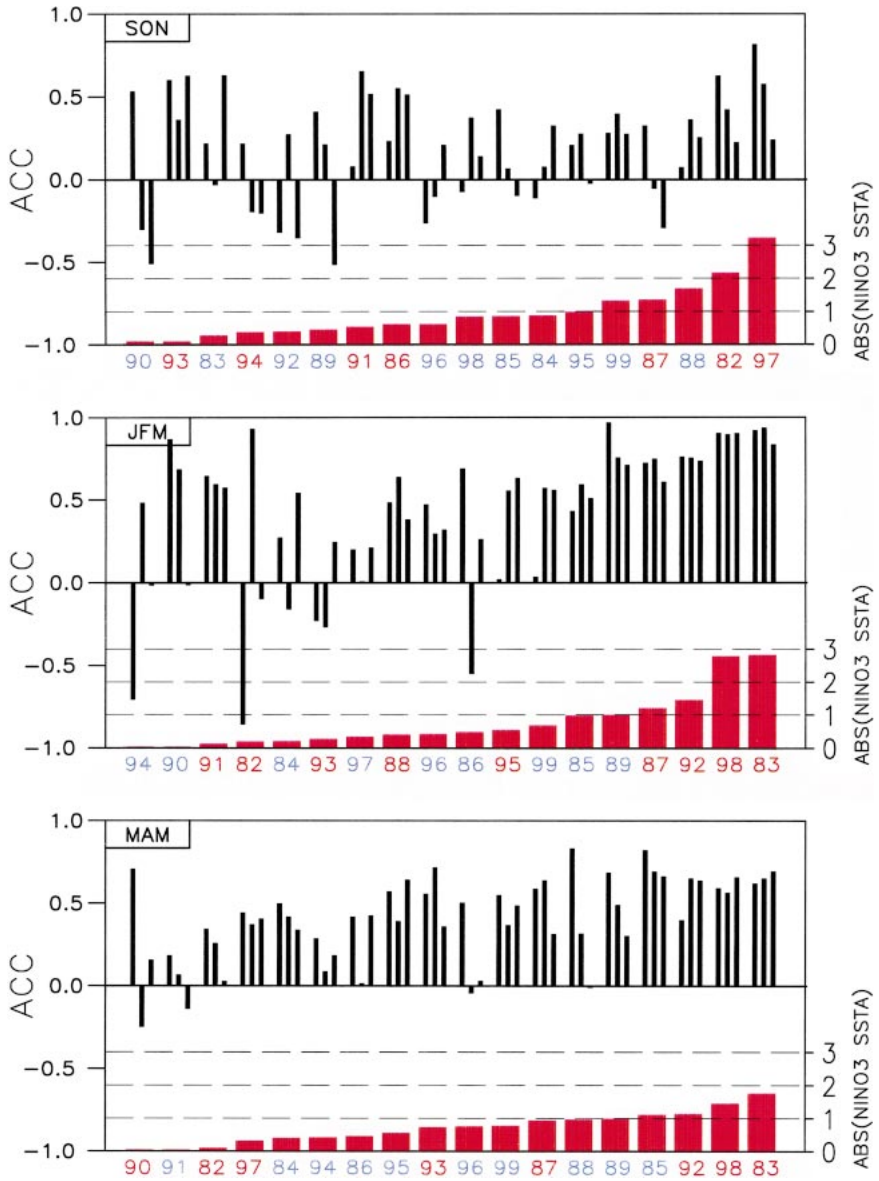

FIG. 1. Each thin vertical bar shows the pattern correlation of the ensemble-mean seasonal-mean 200-hPa height of a GCM with the observed seasonal mean over North America 15°–70°N and 180°–60°W. The pattern correlation is computed separately for each year and for each GCM; the bars show the results for the COLA, NSIPP, and NCEP GCMs from left to right. The years are ordered by the absolute value of the Niño-3 index, increasing to the right and shown by the red bars. Red (blue) numbers indicate warm (cold) years. (top) Results for boreal autumn (Sep–Nov), (middle) for boreal winter (Jan–Mar), and (bottom) for boreal spring (Mar–May).

related to the magnitude of the Niño-3 index (Shukla et al. 2000a), and this is true to some extent for the boreal spring season (shown in the bottom panel). However, the boreal autumn (top panel) shows much less skill and consistency.

In order to be consistent with earlier work describing the midlatitude response to ENSO events (e.g., Chang et al. 2000; Shukla et al. 2000a; Straus and Shukla 2000), we have defined the winter season as the 3-month period of January–March (JFM). Spring is defined as the period from March to May (MAM), and autumn the period from September to November (SON). As a consequence of these definitions, there is a 1-month overlap between winter and spring. We return to this point in section 8.

The results given above are based solely on the Niño-3 index. To explore the boundary forcing more systematically, we analyze the near-global (50°S–50°N) SST anomalies to obtain the dominant patterns of variability and extract the response to these anomalies from the

ensemble GCM simulations. Section 2 describes both the GCMs and observations used, the SST boundary forcing, and the ensembles of seasonal simulations. Section 3 describes a composite analysis of mean precipitation and 200-hPa height based on strong El Niño and La Niña episodes for autumn, winter, and spring seasons. A brief comparison of the methods used to analyze the forced signal is given in section 4, and estimates of the signal and noise variance in 200-hPa height obtained from the different ensembles are discussed in section 5. A nearly global pattern analysis of the SST anomalies is presented in section 6. The tropical precipitation and global height responses of the GCMs to the SST forcing are shown in section 7. A synthesis and the conclusions are presented in section 8.

2. GCM experiments and data

a. GCMs

The three GCMs utilized are those of the Center for Ocean–Land–Atmosphere Studies (COLA), the National Aeronautics and Space Administration (NASA) Seasonal to Interannual Prediction Project (NSIPP), and the National Centers for Environmental Prediction (NCEP). The models are described in more detail in sections 2d–f. Some overall characteristics are given in Table 1.

b. Observed data

The SST used in all GCM simulations, and for the diagnostics in this paper, are the optimal interpolation SST (OISST) data of Reynolds (see Reynolds and Smith 1994). The COLA GCM utilizes the SST data on a weekly basis, while the NSIPP and NCEP GCMs use the monthly SST data. All diagnostics presented use only seasonal means. The observed seasonal mean precipitation is obtained from the Xie–Arkin dataset (Xie and Arkin 1997), while the seasonal mean 200-hPa geopotential heights are obtained from the NCEP reanalysis (Kalnay et al. 1996).

c. Simulations

The boreal autumn simulations were initialized in August and were run through the end of November for the years 1982–99. The number of ensemble members for each GCM is given in Table 1, and the details of the initial conditions are given in sections 2d–f. The boreal winter simulations were initialized in November for the years 1981–98 and were run through the following March. The boreal spring runs were initialized in February of the years 1982–99 and run through June.

d. COLA GCM

This GCM is version 2.2 of the COLA GCM, run at horizontal spectral resolution of triangular T63, with 18 sigma levels. It uses the dynamical core of the National Center for Atmospheric Research (NCAR) Community Climate Model version 3 (CCM3) described in Kiehl et al. (1998); otherwise it is as described in Schneider (2002). The dependent variables of the model are spectrally treated, except the moisture variable, which is advected using the semi-Lagrangian technique. The land surface model (LSM), which is coupled to the atmospheric model, is the simplified version of the Simple Biosphere Model (SSiB) documented in Xue et al. (1991). The parameterization of deep convection is the relaxed Arakawa–Schubert scheme (Moorthi and Suarez 1992). For further details consult Schneider (2002).

There are 10 members in each ensemble. Initial conditions (ICs) 1–5 for the boreal autumn runs are obtained from NCEP reanalyses for 0000 UTC on the last 5 days of August. Initial conditions 6–10 were obtained from ICs 1–5 by adding a perturbation that consists of the difference between the analyses 12 h after and 12 h before. The initial conditions for the boreal winter (spring) runs were obtained in the same manner utilizing the reanalyses for the last 5 days of November (February). The land surface initial conditions were taken from a climatology compatible with SSiB.

Note that because of our definitions of the seasons, (autumn, SON; winter, JFM; spring, MAM), the initial ''spinup'' period for autumn and spring (about 1 month) is shorter than that for winter (about 2 months). This difference also applies to the other ensembles described below. Since we find that differences in daily fields between integrations starting from similar initial conditions saturate in about 2 weeks, the discrepancies in the spinup period should not affect our results.

e. NSIPP GCM

This GCM is the NSIPP-1 atmospheric GCM (AGCM). It uses the gridpoint fourth-order dynamical core of Suarez and Takacs (1995), and was run with a horizontal resolution of 2° latitude $\times$ 2.5° longitude, and with 34 vertical sigma levels. The parameterization of deep convection is the relaxed Arakawa–Schubert scheme (Moorthi and Suarez 1992). For further details consult Bacmeister and Suarez (2002). The atmospheric model is coupled to the Mosaic LSM described by Koster and Suarez (1992).

There are nine members in each ensemble. The ICs for the boreal autumn runs were obtained from the NCEP reanalyses at 0000 UTC 13–17 August and at 1200 UTC 13–16 August. The ICs for the boreal winter (spring) runs were obtained in the same manner utilizing the reanalyses for 13–17 November (February). The land surface initial condition for each ensemble member and for all years of the boreal winter runs was taken from a single arbitrary December state from a previous experiment. Simulations for the boreal autumn and spring seasons took the land surface IC from a previous multiyear continuous simulation made with observed

SSTs, using the corresponding month and year. (Thus for the autumn and spring runs, the land initial states can potentially contribute to the forecast skill indirectly through the SST that forced the previous runs.)

f. NCEP GCM

This GCM is the NCEP Seasonal Forecast Model (Kanamitsu et al. 2002). The model is a spectral model with triangular resolution of T62, with 28 sigma levels in the vertical. It utilizes the same parameterization of deep convection as the COLA and NSIPP GCMs. The land processes are represented by the two-layer LSM of Pan and Mahrt (1987). Further details are given in Kanamitsu et al. (2002).

There are 10 members in each ensemble. The ICs for the boreal autumn runs were obtained from the NCEP reanalyses at 0000 and 1200 UTC 1–5 September. The ICs for the boreal winter (spring) runs were obtained in the same manner utilizing the reanalyses for 1–5 November (February). The land surface conditions were taken from a climatology compatible with the land surface model.

Note that the length of the spinup period is not consistent from model to model. With the exception of the COLA GCM simulations for SON and MAM, these periods are all longer than 2 weeks. We do not expect a major impact on our findings from this inconsistency.

3. The ENSO-related global signal

Composite seasonal means for the boreal autumn, winter, and spring seasons based on the traditional wintertime ENSO framework serve as a useful reference. The three winters with the highest values of Niño-3 (JFM 1983, 1998, 1992) are defined as warm winters, while those with the lowest values of Niño-3 (JFM 1989, 1985, 1999) are defined as cold winters (see Fig. 1). The autumns preceding these winters and the springs following them are considered to be part of the three warm and three cold episodes, even though they do not necessarily have the largest magnitude of Niño-3. Subtracting the average of a seasonal mean field over the three cold episodes from the average of that field over the three warm episodes gives a simple composite measure of the warm-minus-cold anomalies.

The composite SST warm-minus-cold differences are shown by the contours in Fig. 2, while the shading indicates regions where the winter-averaged SST for the warm events exceeds 28°C, giving a rough indication of where conditions are favorable for convective activity. While autumn (Fig. 2a) SST anomalies are as large as during winter over much of the eastern Pacific, the temperature along the equator in autumn east of 135°W is too low to support convection even in the warm years. Conversely, while the spring anomalies over much of the eastern equatorial Pacific are smaller than their winter counterparts, the water is warm enough to support convection along the equator right up to the South American coast. Here the winter (spring) anomalies exceed 3°(4°)C.

Figure 3 shows the corresponding differences for the observed precipitation over the tropical Pacific basin. (The shading denotes 95% statistical significance based on the *t* test.) The winter anomaly (middle panel) shows the familiar ENSO signal, with largest positive anomalies just east of the date line and an eastward extension along the equator right up to the coast of South America. The springtime precipitation anomaly (bottom panel) is very similar in structure to that in the preceding winter, with a somewhat reduced magnitude in the central Pacific. The equatorial anomalies in the eastern Pacific are just as strong as in winter. In contrast, the preceding autumn's composite anomaly (top panel) is considerably weaker east of 120°W, especially along the equator, consistent with the position of the 28°C isotherm in Fig. 2. The autumn anomalies near the date line are as strong as in spring. In all seasons, negative anomalies are seen poleward of about 10° in both hemispheres in the central Pacific and in the western Pacific.

The corresponding GCM seasonal mean, warm-minus-cold precipitation anomalies are shown in Fig. 4. Here we have averaged the seasonal mean composites over all members of the ensembles and over the three GCMs. The main conclusions gleaned from the observations are unchanged: the spring warm-minus-cold composite is as strong in the eastern Pacific along the equator as in winter, while the autumn composite difference is smaller here. However, the GCMs do show a somewhat stronger than observed precipitation anomaly in the central Pacific during spring.

Unfortunately, there is a paucity of published GCM data with which to compare the SON and MAM panels of Fig. 4. Kumar and Hoerling (1998) note that the rms errors of tropical precipitation in their GCM during March and April (and also during October and November) are nearly as large as those during December–February. Bates et al. (2001) report a wide range of tropical precipitation errors seen in three GCMs during the April–June seasons, both in terms of patterns and magnitude.

The warm-minus-cold composites for the global 200-hPa height field obtained from reanalyses are shown in Fig. 5. The winter warm-minus-cold composite shows the expected dramatic height rise in the tropical Pacific, the well-known ENSO response pattern over the Pacific–North American (Pac–NA) region (see, e.g., Straus and Shukla 2000, 2002), and a quite well-defined wave train in the Southern Hemisphere. In addition, a high-latitude dipole over the North Atlantic region and a midlatitude dipole over east Asia are seen. The following spring height composites contain many of the same basic structures, although with a reduced magnitude and with a distinct shift in the enhanced Aleutian low. The anomalies over the Pac–NA region nearly disappear in the preceding autumn, although the Southern Hemi-

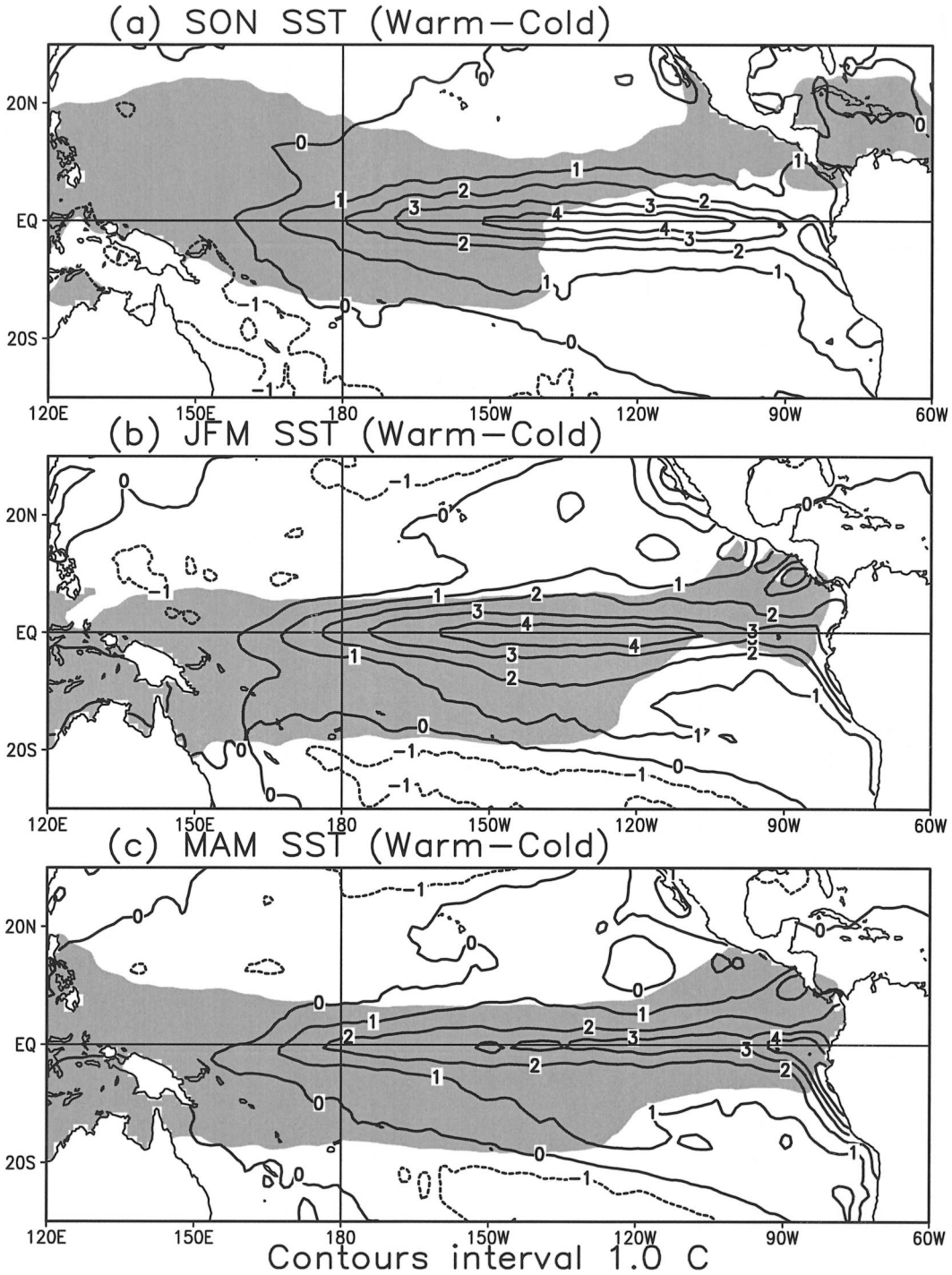

FIG. 2. Warm-minus-cold composite seasonal mean SST, in °C. Shading indicates regions where the composite warm SST exceeds 28°C. The warm and cold composites are taken over years based on the value of the Niño-3 index for boreal winter; the winter definition applies to the preceding autumn and following spring. (a) Autumn, (b) winter, and (c) spring composite differences.

sphere response and the dipoles over the North Atlantic and east Asia are discernible. The GCM composite 200-hPa height response is shown in Fig. 6, averaged as before over the ensembles of all three GCMs. The main tropical, Pac–NA region and Southern Hemisphere observed features are all clearly seen in the mean GCM results, as well as the low over subtropical east Asia. During spring, an anomalous high over North America

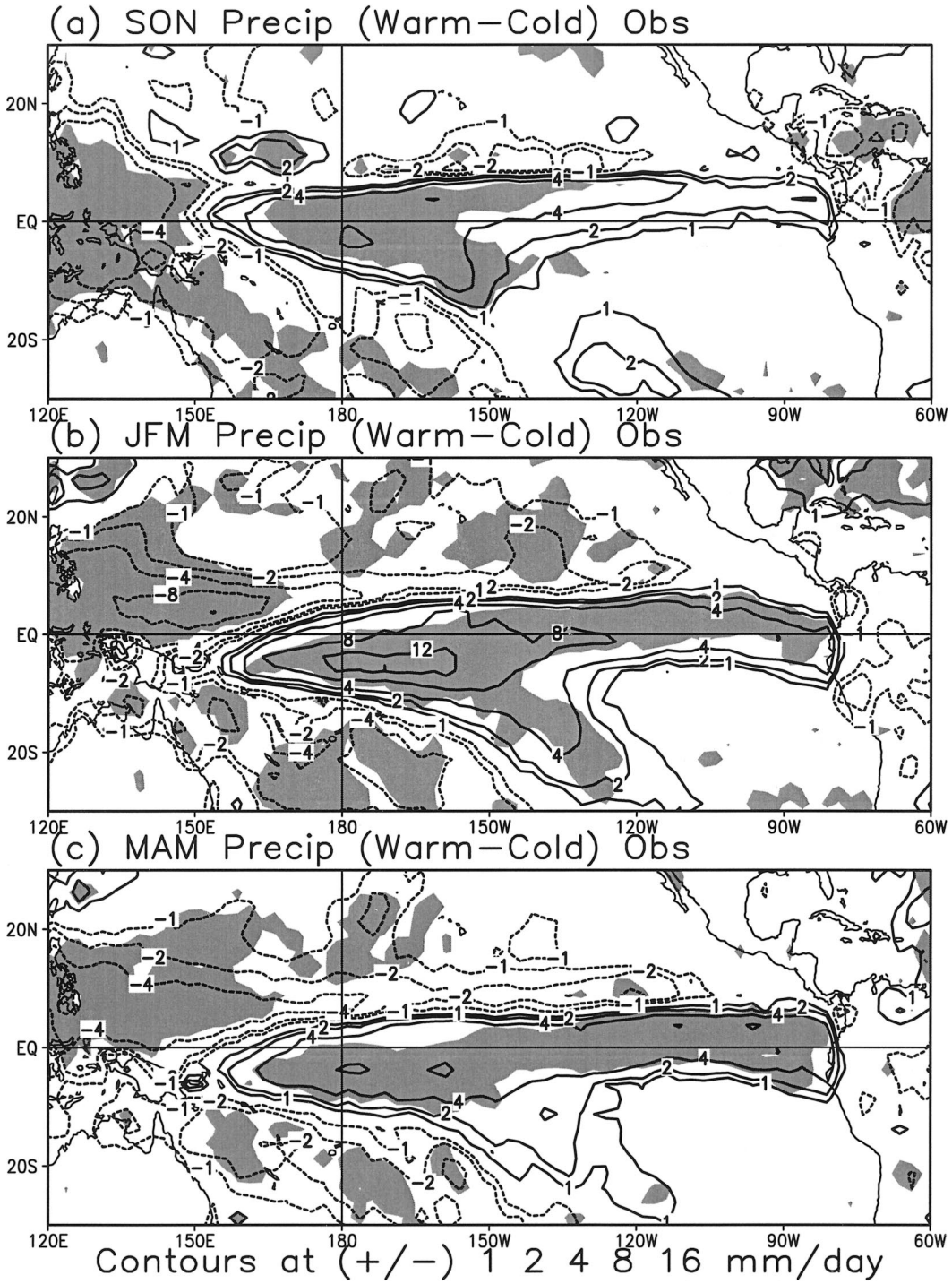

FIG. 3. Warm-minus-cold composite seasonal-mean observed precipitation (Xie and Arkin 1997), in units of mm day^{-1}. Contours drawn at $\pm$1, 2, 4, 8, 12, and 16 mm day^{-1}. Shading denotes significance at the 95% confidence level. The warm and cold composites are taken over years based on value of the Niño-3 index for boreal winter; the winter definition applies to the preceding autumn and following spring. (a) Autumn, (b) winter, and (c) spring composite differences.

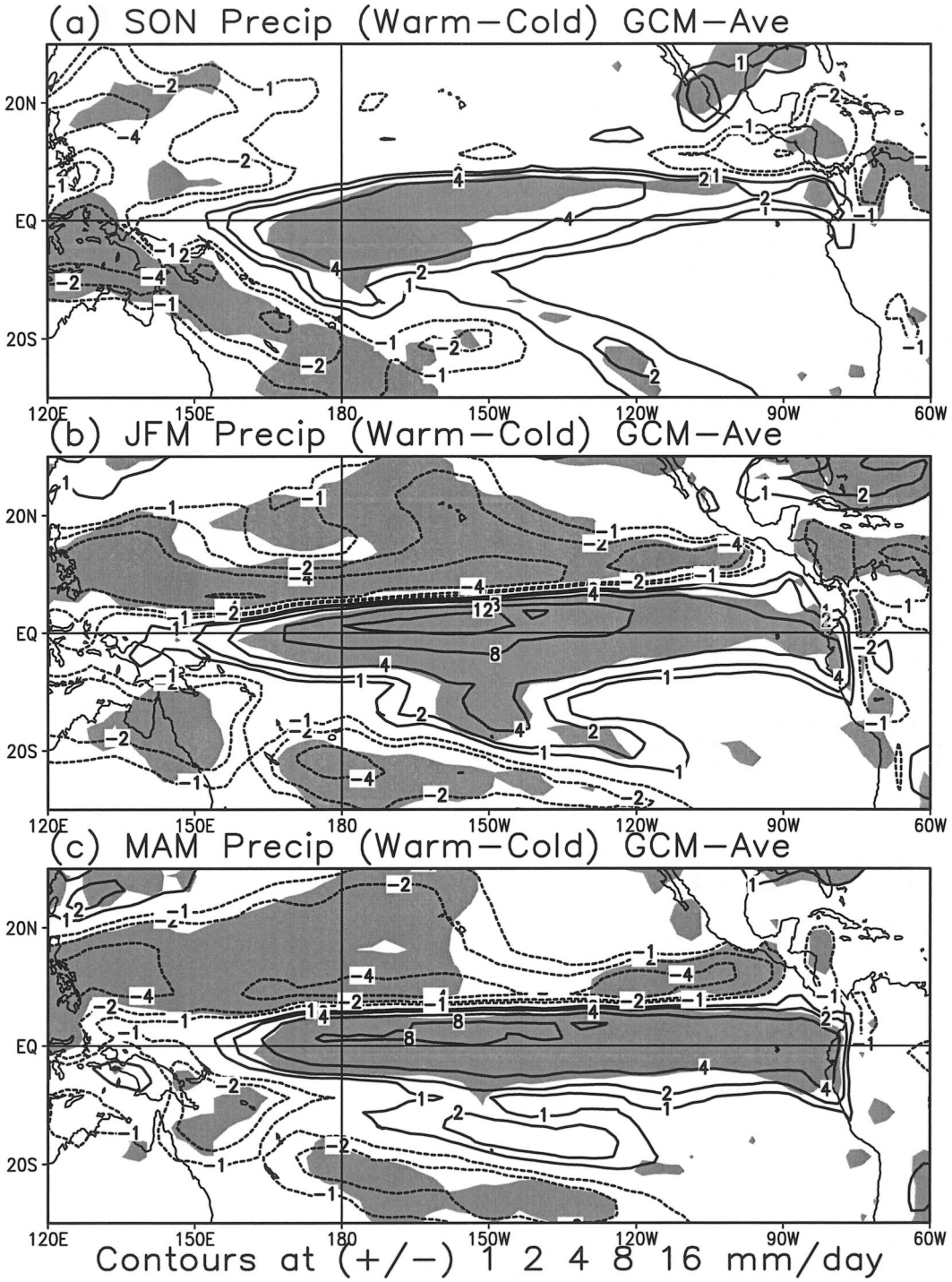

FIG. 4. As in Fig. 3, except for the average of three GCM ensemble means.

now appears, although it is not seen in the observations. The zonally symmetric anomalies suggested by the observations and found even more clearly in the GCM results have been pointed out before (Hoerling et al. 1995).

These preliminary results suggest that while the spring looks in some sense like a weaker version of winter (with some of the Northern Hemisphere features shifted), the autumn response to tropical SST forcing is fundamentally different. While this ENSO-oriented analysis derived from the Niño-3 index is useful, the

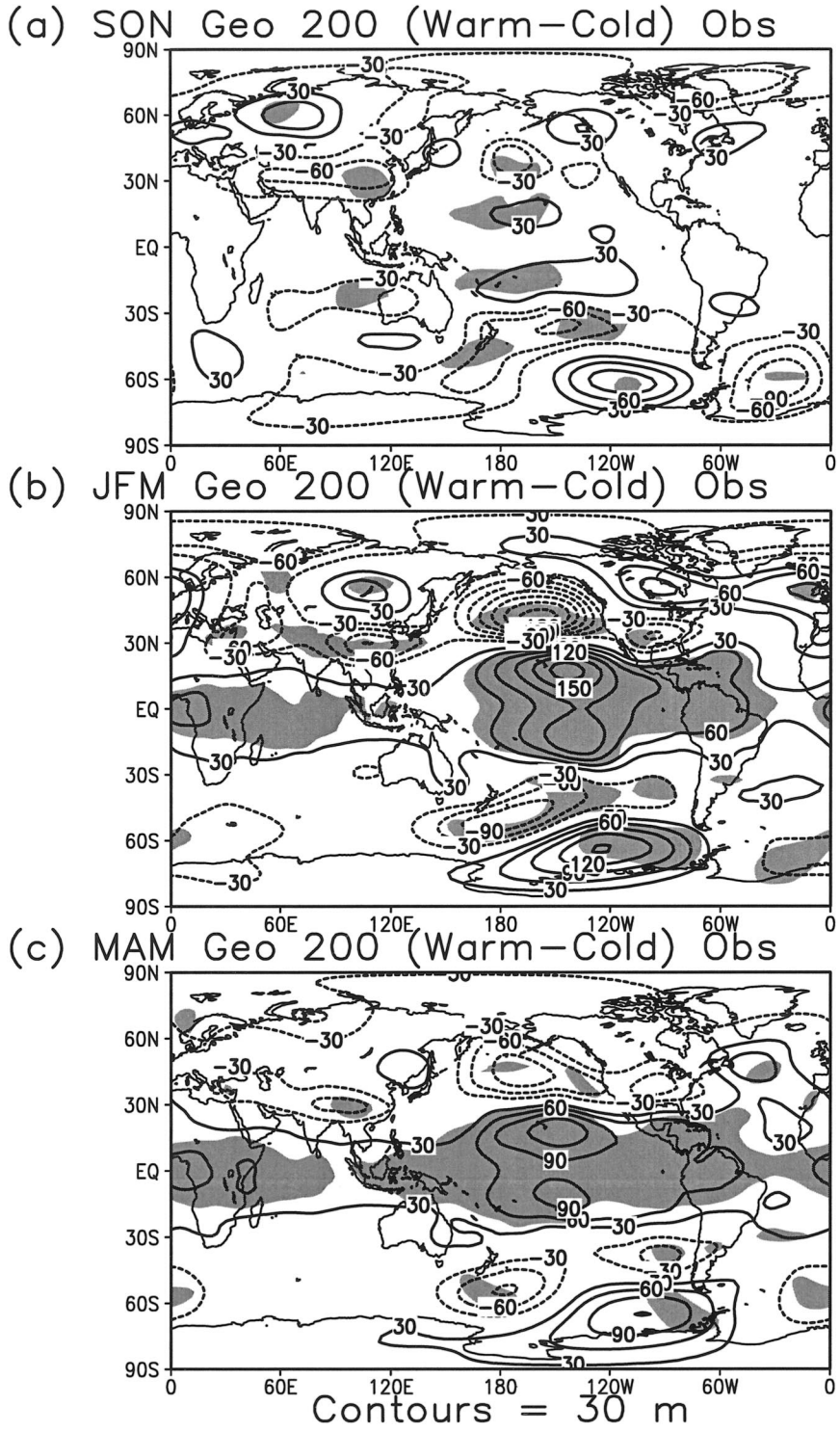

FIG. 5. Warm-minus-cold composite seasonal-mean 200-hPa height in units of m. Contour interval is 30 m. Shading denotes significance at the 95% confidence level. The warm and cold composites are taken over years based on the value of the Niño-3 index for boreal winter; the winter definition applies to the preceding autumn and following spring. (a) Autumn, (b) winter, and (c) spring composite differences.

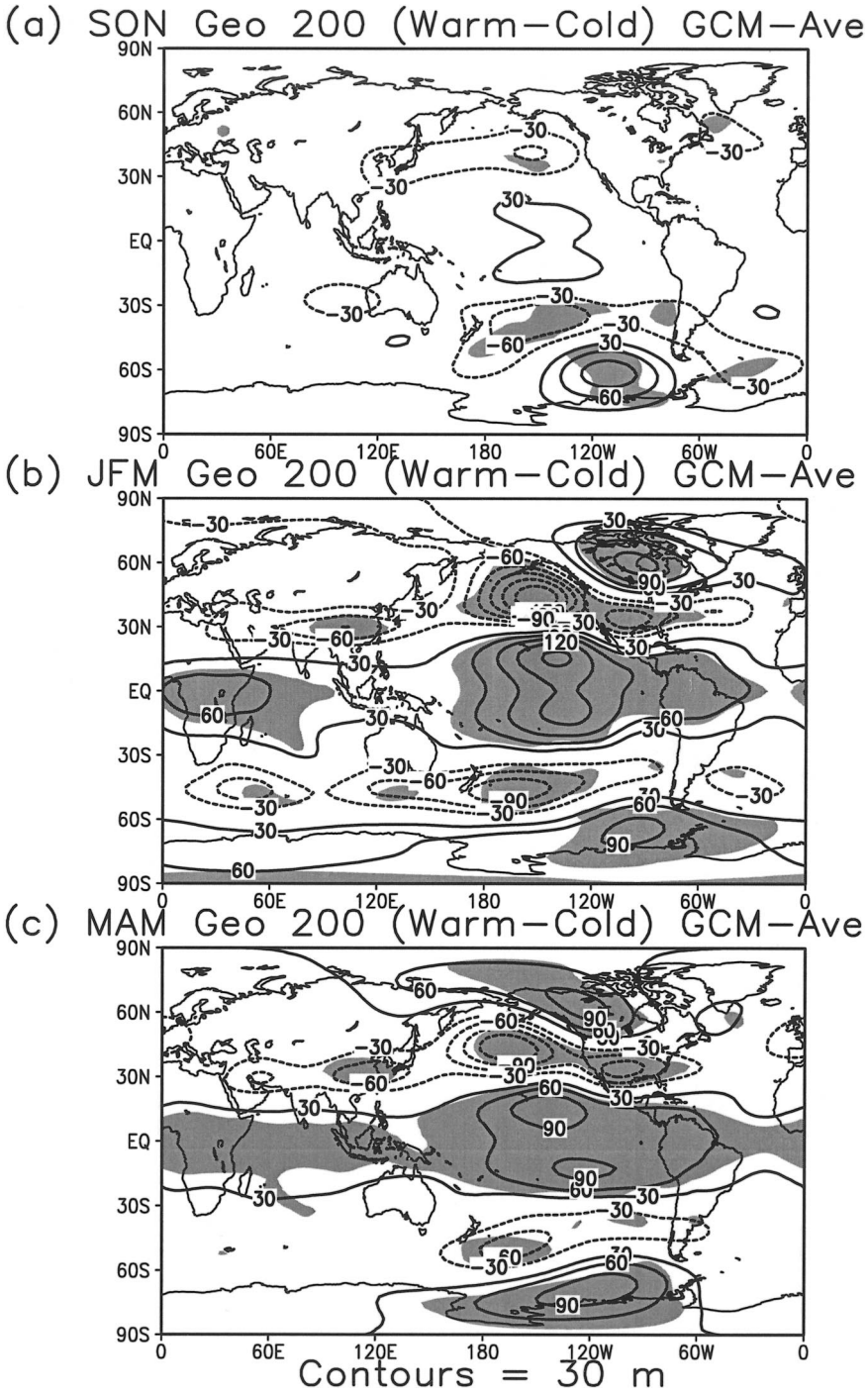

FIG. 6. As in Fig. 5, except for the average of three GCM ensemble means.

weak autumn response suggests we should look to other tropical SST anomaly signals.

4. Measures of response to external forcing

Since this paper uses a number of techniques to estimate the observed and simulated response to SST variations, it is useful to compare the properties of and assumptions made by the various methods.

a. Signal and noise variance

Ensemble GCM experiments allow us to separate the forced SST response from the variability of seasonal

means due to internal chaotic dynamics. The overall level of internal variability (the noise variance) can be estimated from the average intraensemble variance, while a measure of the SST-forced signal is the temporal variance of the ensemble mean, corrected for the presence of noise (see Scheffé 1959, p. 225; also Rowell et al. 1995; Straus and Shukla 2000). Maps of these variances and the signal-to-noise ratio indicate where the overall signal dominates the noise; however, in contrast to methods outlined in sections 4b–d below, individual patterns of response are not indicated. Note that no assumption has been made regarding which features (spatial or temporal) of the underlying SST are important in producing the response; in fact the SST field does not enter explicitly at all. This technique clearly cannot be applied to observations.

b. Composite analysis

Used in section 3, this technique assumes that we can distill those features of the forcing (in this case SST) that are important in producing a response into a single index (here the seasonal mean value of Niño-3). Composites refer to averages of the desired (ensemble mean) response fields (precipitation, height) over periods in which the index lies in extreme values. Differences between the positive and negative composites yield measures of the response to extreme differences in the forcing, but no assumption of linearity in the forcing index is made. The significance level of the composite patterns can be assessed locally by a *t* test.

c. Linear regression

Here we also assume that we can distill the forcing into a single time series. (In section 7a, this time series is given by the leading principal component of the seasonal mean SST field.) The regression of the response fields onto this index gives that portion of the response that is linearly related to the forcing time series. Note that the ensemble mean fields for all years are used, in contrast to composite analysis. The significance level of the regression patterns can be assessed locally by a *t* test.

d. Signal-to-noise optimal patterns

This method, equivalent to the signal detection technique discussed in Venzke et al. (1999), seeks to find those patterns that maximize the signal-to-noise ratio. For each pattern, the signal is defined as the temporal variance of the ensemble mean of the time series associated with that pattern, and the noise is defined as the average intraensemble variance of the time series (see the appendix for details). As opposed to composite and regression analysis, this method utilizes all the ensemble members (not just the ensemble mean). As in section 4a, no assumptions are made about what characteristics of the prescribed SST fields are important for the response, and no explicit information about the SST even enters into the calculation. In this technique, the patterns are ordered by their signal-to-noise ratio, with the leading pattern having the largest ratio. Significance tests for the ratio are discussed in the appendix, as well as a measure of the local significance of the associated patterns. Clearly this method is not applicable to observations.

An alternative technique to the optimal approach is to compute the empirical orthogonal functions (EOFs) of the ensemble-mean seasonal-mean fields, as in Straus and Shukla (2000, 2002). This does not utilize the ensemble spread information; the leading EOF tends to be similar to the leading optimal pattern (not shown).

5. Signal and noise variance

The signal variance of the seasonal-mean 200-hPa height, the internal (noise) variance, and their ratio are shown in Fig. 7 for the three GCMs for boreal autumn. The signal variance (shown in Figs. 7a–c) consistently shows a large signal in the Southern Hemisphere and a smaller signal over the Pacific and east Asia in all three GCMs. The signal over North America is very weak. The noise variance (shown in Figs. 7d–f) is also consistently large in these same regions, leading to a generally weak signal-to-noise ratio outside the Tropics in all three GCMs. This dimensionless ratio is shown in Figs. 7g–i. Significance at the 95% level is shown by the shading. The significance test we use refers to rejecting the null hypothesis that the signal-to-noise ratio $r \leq 1$, which leads to a stricter test than that commonly used null hypothesis ($r = 0$). See Scheffé (1959, p. 227) for the calculation of significance. Outside the Tropics, only the subtropical southern Pacific shows a ratio that is significant.

The corresponding results for boreal winter (spring) are shown in Fig. 8 (Fig. 9). For spring, all three GCMs have strong signals in the Pacific and over North America, in the southern Pacific, and even in the Tropics, the latter reflecting the overall warming of the Tropics during warm events. Again, the noise tends to be strongest where the signal is strongest, but now the ratio is significantly larger than 1.0 over subtropical North America, and for the NCEP GCM over the midlatitude Pacific as well. As before, highly significant ratios are seen over the Tropics, indicating very little noise there.

The autumn and spring results should be put into the context of the boreal winter variances given in Fig. 8. (Note the differences in the contours used.) The winter signal variances are stronger than either transition season, with the large signals over the Pac–NA region dominating the Tropics and Southern Hemisphere. The North Pacific is also a region of large noise (particular in the COLA GCM), yet the ratio is still significantly greater than 1.0 in the northeast Pacific and over the subtropical North American continent.

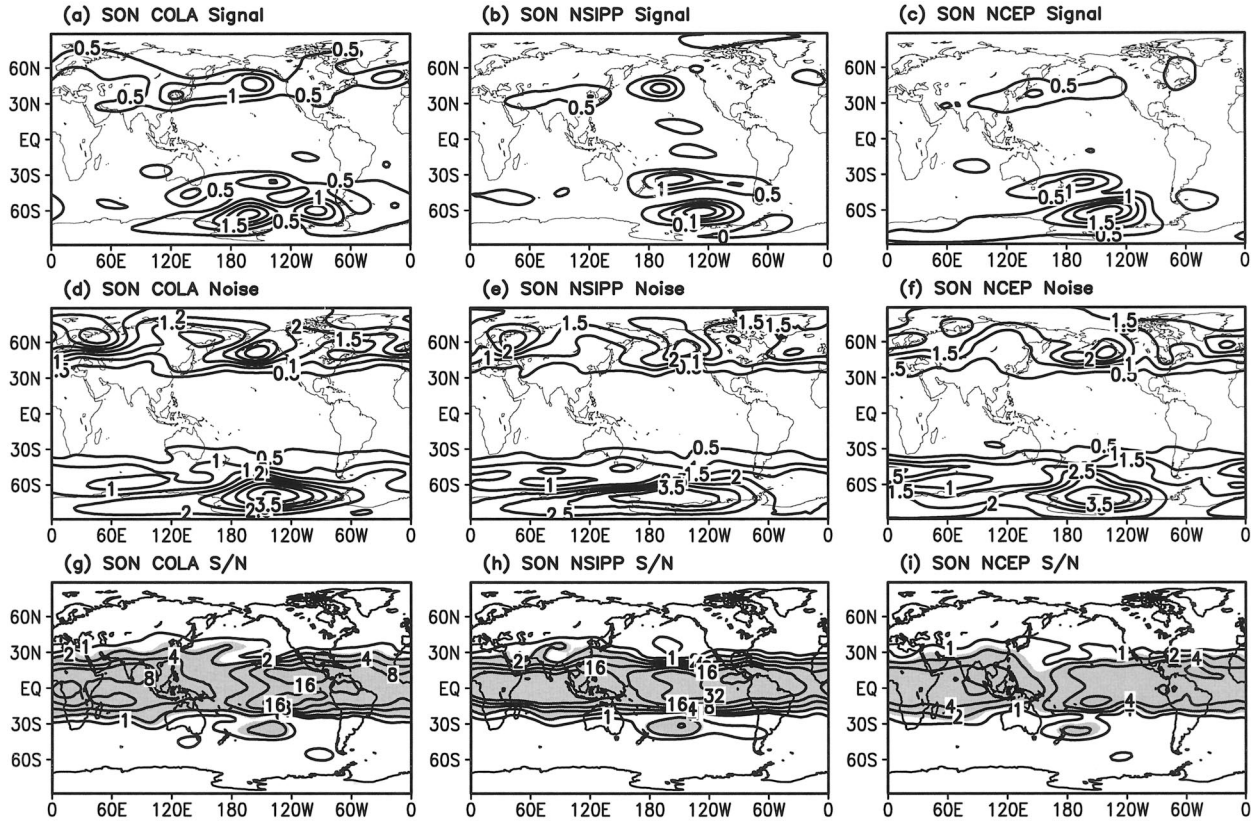

FIG. 7. (a)–(c) Signal variance, (d)–(f) noise variance, and (g)–(i) signal-to-noise ratio for three GCMs for boreal autumn. Contour interval is 0.5×10^3 m^2 in (a)–(f). Dimensionless contours of 1, 2, 4, 8, 16, 32, and 64 in (g)–(i). Shading in (g)–(i) indicates 95% significance.

Some model dependence to the signal and noise variances can be seen in Figs. 7–9. In particular the COLA GCM tends to have a larger noise variance, especially over the Pacific during winter. In addition, the NCEP GCM has much lower signal-to-noise ratios in the Tropics than do the other GCMs. The lower ratios are due to enhanced tropical noise in the height field, which is unlikely to impact the results shown in later sections. It should be noted that the discrepancies are in general less than those shown for an earlier generation of models used in Shukla et al. (2000a) indicating some convergence may have been achieved. We return to this point in the discussion.

6. SST patterns

In order to objectively organize the dominant seasonal mean patterns of SST forcing, we have performed a rotated empirical orthogonal function (REOF) analysis of the near-global (50°S–50°N) SST anomalies. We excluded the high latitudes from the analysis to avoid dealing with sea ice effects, which are not well handled by the GCMs. For boreal spring and winter there is a large difference in the cumulative globally averaged temporal variance explained by the first two REOF patterns, with the leading REOF associated with three times the variance of REOF-2 (see Table 2). In boreal autumn the variances explained by the leading two REOFs are closer (31% versus 19%), so we consider both modes. Figure 10 shows these two REOF patterns, as well as the leading REOF patterns for boreal winter and spring. The leading pattern for all three seasons is dominated by warming in the eastern Pacific, with the winter pattern corresponding to the classic ENSO signal and the transition season patterns having a maximum just off the South American coast. This large eastern tropical Pacific weighting leads to a large correlation with the Niño-3 index (see Table 3), and the corresponding principal component (PC) time series have peaks during the strong ENSO episodes of SON/JFM/MAM 1982/83, 1986/87, 1988/89, 1991/92, and 1997/98 (not shown). The second REOF pattern for autumn has a broad maximum in the central Pacific, and a strong positive anomaly in the North Pacific. Its PC time series is not well correlated with Niño-3. (Whether or not this mode of SST is itself predictable is an open question.) Since the warmest waters are generally confined to the central tropical Pacific during autumn (as seen in Fig. 2), this mode of SST is expected to be important for forcing an atmospheric response. The two patterns shown for autumn are quite similar to those shown by S2 for boreal summer (their Fig. 6).

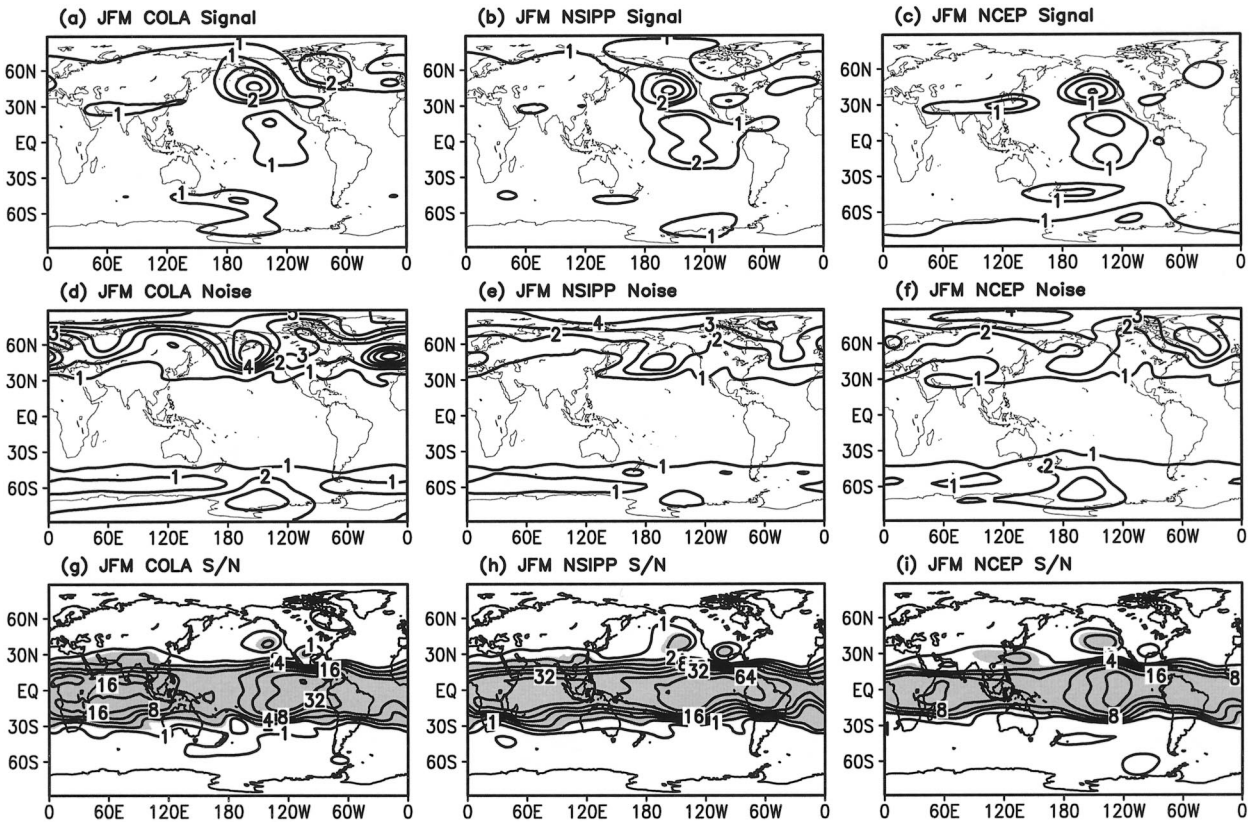

FIG. 8. (a)–(c) Signal variance, (d)–(f) noise variance, and (g)–(i) signal-to-noise ratio for three GCMs for boreal winter. Contour interval is 2.0×10^3 m^2 in (a)–(c), and 1.0×10^3 m^2 in (d)–(f). Otherwise as in Fig. 7.

7. Response of precipitation and global height

a. Precipitation

The linear response of seasonal mean precipitation to the dominant pattern of SST during JFM and MAM is obtained by linear regression of this field on the PCs of SST. For the GCMs, the regression is done using the ensemble means. The results (not shown) are consistent with the warm-minus-cold composites seen in Figs. 3 and 4. The two seasons show a similar response dominated by positive anomalies over the central and eastern equatorial Pacific, with negative anomalies surrounding this to the north, south, and west in a characteristic ''horseshoe'' shape. The peak magnitude of the boreal spring response is somewhat smaller than in winter, consistent with the composites.

The linear responses of the SON ensemble mean precipitation to the two leading SST REOF patterns is estimated by regression of the means on PC-1 and PC-2. Figure 11 shows the observed regression pattern and the average of the regression patterns obtained from the three GCMs. Significance at the 95% level is indicated by shading. The regression on PC-1 is similar to the Niño-3 composites shown earlier, with a dominant central Pacific positive anomaly that weakens as it extends toward the South American coast. The regression on PC-2 has some similarity to that for PC-1, but the dominant positive anomaly in the tropical Pacific is more closely confined to the date line. The strong negative anomaly appearing north of the equator in the western Pacific in the observations is shifted to the north in the GCMs.

The leading optimal signal-to-noise patterns for precipitation were calculated for all three seasons and for all three GCMs. The leading patterns for all seasons (not shown) agree quite well with the corresponding regression patterns on PC-1. The second optimal pattern for autumn also agrees with the regression on PC-2 of SST during autumn. The overall agreement between the response patterns as estimated by these two methods (even if the magnitudes differ somewhat) indicates that the tropical linear responses to the leading modes of SST are associated with high signal-to-noise ratios.

b. 200-hPa height

The leading optimal patterns in seasonal-mean 200-hPa height for boreal winter and spring are shown in Figs. 12 and 13 for the three GCMs. The signal-to-noise ratios indicated in the figures correspond to a truncation of 10 EOFs; the ratios in parentheses to a truncation of 20 EOFs. The shading in the figures indicates regions

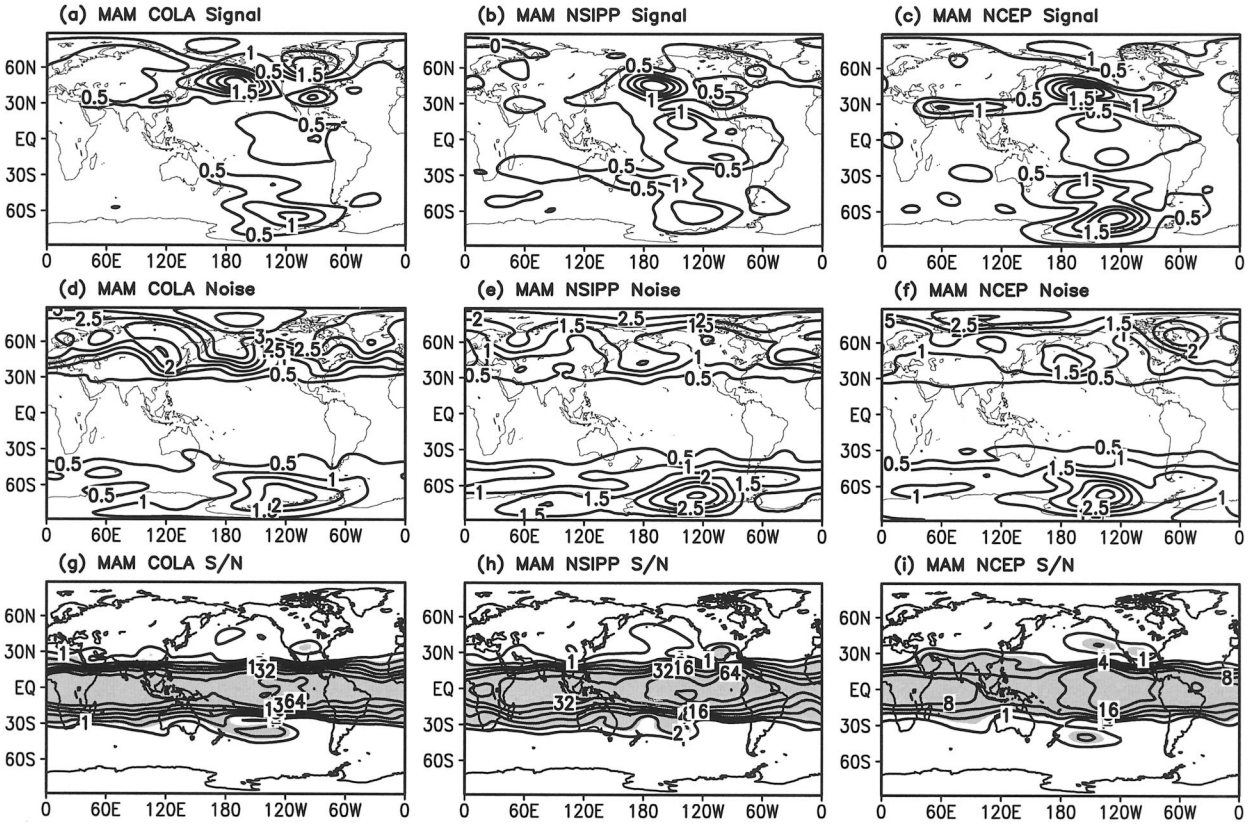

FIG. 9. As in Fig. 7, but for boreal spring.

where the optimal pattern ''explains'' at least 50% of the total ensemble-mean variance. Readers are referred to the appendix for more technical detail.

The models all show the expected tropical warming (particularly in the eastern Pacific) for both seasons, and well-defined wave trains in both hemispheres in the 180°–300°E longitude belt. The spring pattern for each GCM is very similar in structure to the corresponding winter pattern, but with a smaller amplitude and with systematic shifts in northern midlatitudes. The winter maps in the Pacific–North American region look very similar to the ENSO-related pattern familiar from the recent literature (see, e.g., Straus and Shukla 2000, 2002 for maps and references). The enhanced Aleutian low, the subtropical low over continental North America, and the high over northeastern Canada are present in all maps. In general the COLA and NSIPP GCMs' responses are very similar; the NCEP GCM differs in producing a weaker and slightly displaced Canadian high, and a quite strong and broad subtropical response over Asia. Not only do all the models show a weaker response in spring than in winter, but both the low over the North Pacific and the Canadian high are shifted westward consistently in the models.

TABLE 2. Percentage of total variance associated with rotated EOFs of SST, labeled as PctVar.

Season	Mode *n*	PctVar (%)
SON	1	31.3
SON	2	19.3
JFM	1	33.1
JFM	2	9.4
MAM	1	28.5
MAM	2	11.8

The optimal patterns account for at least half the variance of the ensemble means in the Tropics and in the wave trains in both hemispheres, as indicated by the shading in Figs. 12 and 13. (In the MAM results for the COLA model, the optimal pattern explains only 30% of the ensemble-mean variance over the Aleutian low.)

In order to determine whether these optimal patterns are consistent with the assumption of linearity with respect to the PCs of SST, we computed the serial correlation coefficient of the time series associated with the leading optimal pattern with the SST PC for boreal winter and spring. The results (see Table 4) show very high values of the correlation (exceeding 0.90 in all cases), indicating that these patterns can, to a good approximation, be thought of as linear responses to the SST forcing patterns represented in Figs. 10c and 10d. As would be expected, the linear regression of the ensemble-mean height fields on the leading SST PC for winter

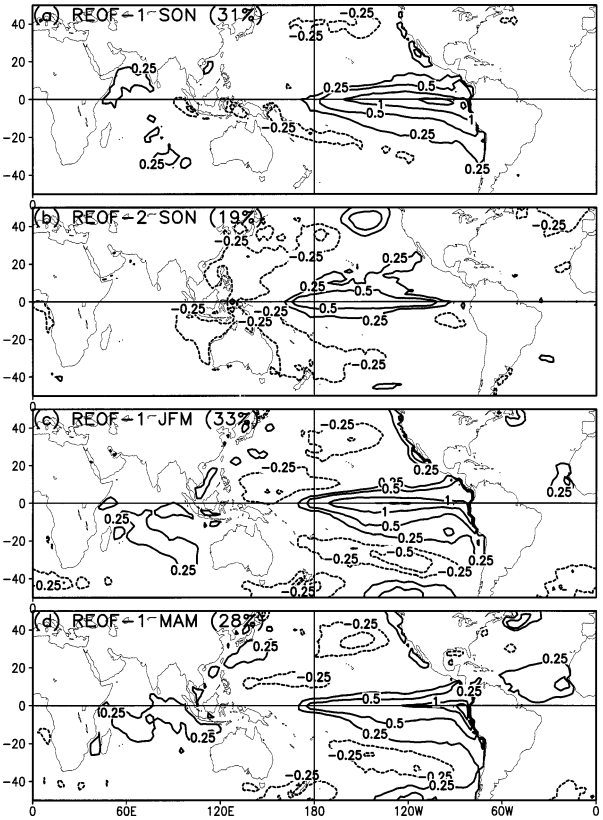

FIG. 10. (a), (b) Two leading REOFs of the seasonal-mean SST field for boreal autumn, (c) leading REOF for boreal winter, and (d) for boreal spring. Patterns are dimensional, corresponding to the associated time series having unit variance. Contour interval is 0.25°C. Percentages in parantheses are explained in the text.

and spring (not shown) yields patterns very similar to those shown in Figs. 12 and 13.

The results for boreal autumn are quite different. The leading two optimal modes are shown for all GCMs in Figs. 14 and 15. The leading optimal mode has very weak features (note the contour interval in Fig. 14). For the COLA and NSIPP GCMs a nearly uniform tropical warming dominates, with a remnant of some of the midlatitude winter and spring features appearing. The NCEP GCM shows a nearly uniform global warming. The optimal pattern for all three GCMs accounts for over half the variance of the ensemble means in the Tropics only.

The second optimal pattern, defined as the pattern that optimizes the signal-to-noise ratio subject to the constraint that it is independent of the first pattern, bears some similarity to the boreal spring responses. In particular, the enhanced Aleutian low, along with its extension westward into east Asia, are seen in all GCMs, and even a weak eastward extension across southern North America is noted in the COLA and NSIPP responses. The Southern Hemisphere wave trains are stronger than in either winter or spring, and are slightly shifted both westward and toward the equator. This pattern accounts for over half the ensemble-mean variance in the extratropics only.

TABLE 3. Correlation (corr) between the SST PC associated with rotated EOF mode *n* and the Niño-3 index.

Season	Mode *n*	Corr
SON	1	0.93
SON	2	0.34
JFM	1	0.98
MAM	1	0.91

The interpretation of each of these patterns in terms of SST forcing is facilitated by noting that there is a strong correlation between PC-1 of the SST field and the time series associated with the leading optimal mode for all GCMs for boreal winter and spring. For SON, this correlation exceeds 0.70 for the leading two optimal modes (and corresponding PCs) for the COLA and NSIPP GCMs. This high degree of correlation could not have been assumed a priori, since the optimal analysis uses no explicit SST information.

The notion that only a generalized warming (or cooling) of the tropical belt is forced by the leading SST pattern in SON is consistent with Fig. 2, which implies

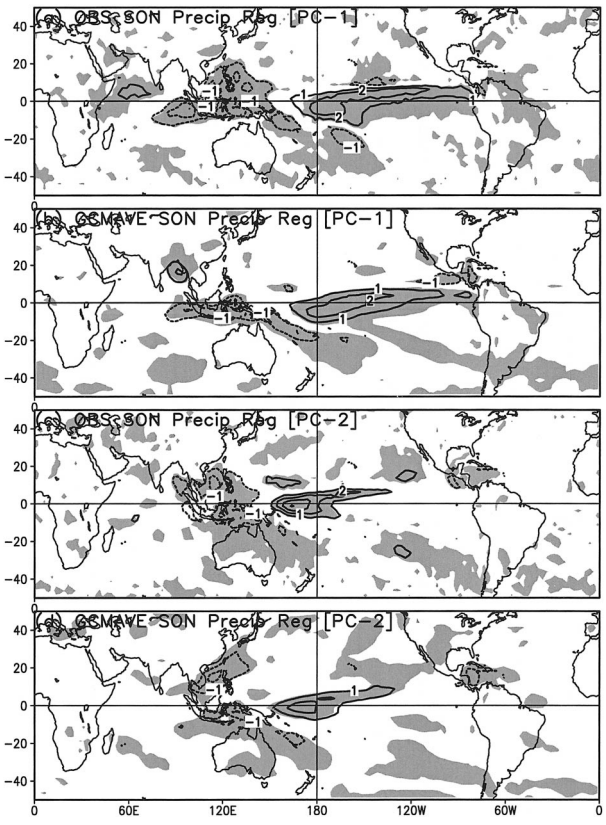

FIG. 11. Regression coefficients of seasonal-mean precipitation on (a), (b) PC-1 of SST and on (c), (d) PC-2 for boreal autumn, for (a), (c) observations and for (b), (d) the average of the three GCMs. The shading indicates the 95% significance level. Regression coefficients have a contour interval of 1 mm day^{-1} °C^{-1}.

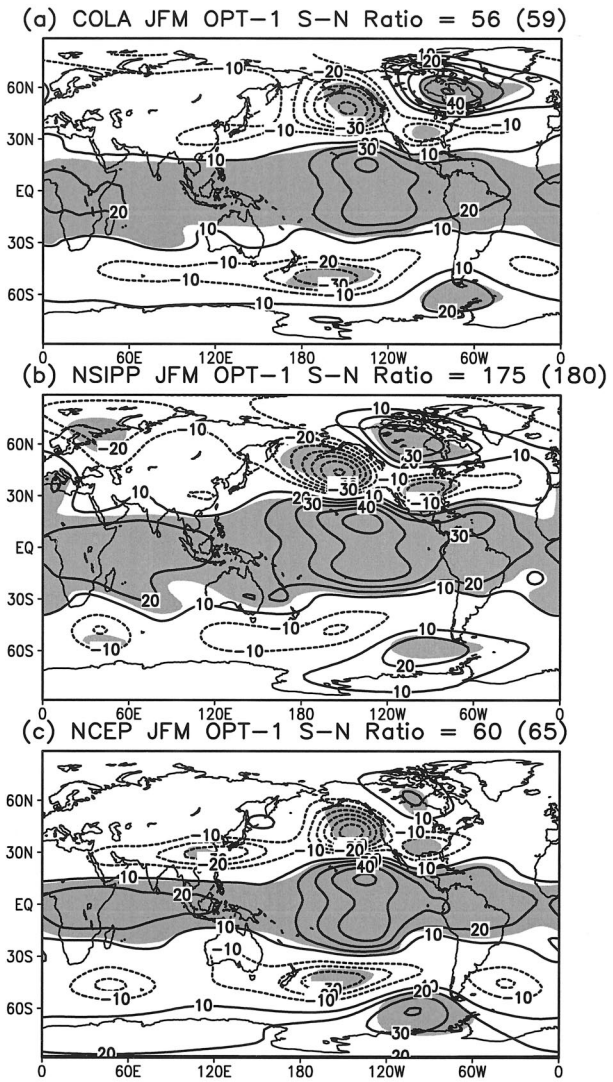

FIG. 12. The leading optimal signal to noise pattern of 200-hPa height for the COLA, NSIPP, and NCEP GCMs for the boreal winter. Shading denotes regions where the optimal mode explains greater than 50% of the ensemble-mean variance. Contour interval is 10 m.

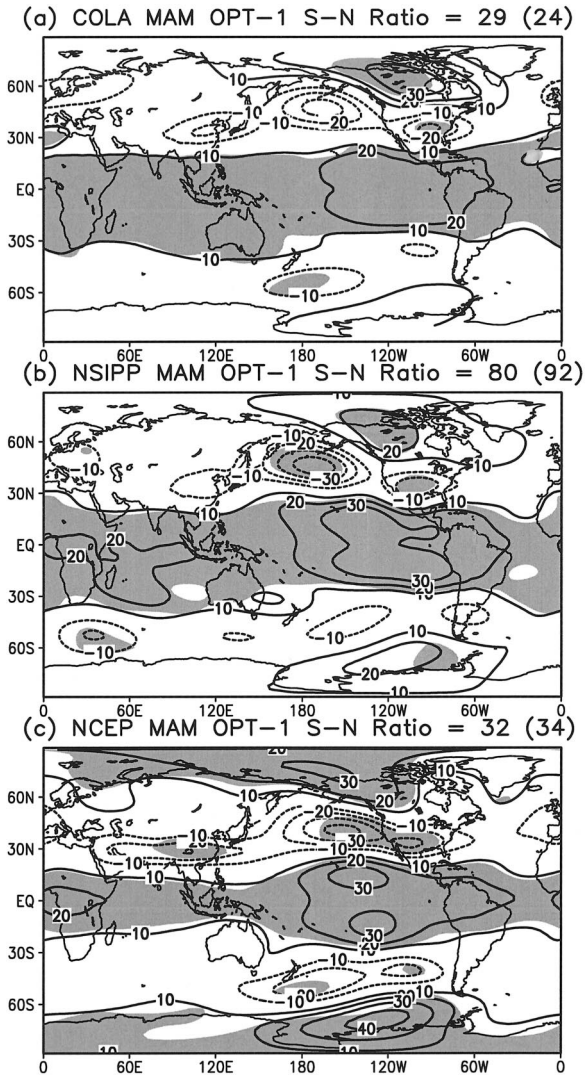

FIG. 13. As in Fig. 12 but for boreal spring.

that strong regional convective forcing in the eastern Pacific cannot be effective on the seasonal-mean timescale. When convective forcing does occur in the central Pacific, as in the second SST pattern, it is associated with wave trains in both hemispheres. While the particularly strong central Pacific wave train in the Southern Hemisphere (during austral spring) is interesting as an example of a forced stationary response, it also may have some practical value for seasonal forecasts over New Zealand.

It is noteworthy that the boreal autumn height response seen here bears some similarity to ensemble GCM results obtained for summer using the NSIPP-1 GCM (see S2). As mentioned earlier, the leading two EOFs of SST shown in S2 (their Fig. 6) bear a strong similarity to our Fig. 10a and 10b: the leading EOF is dominated by warm SST in the far eastern tropical Pacific, with some Indian Ocean signal, while the second EOF shows the dominant warming in the central Pacific. The boreal summer mean 200-hPa-height responses obtained by S2 using linear regression on the SST PCs (and shown in their Fig. 9) bear some similarity to Figs. 14 and 15. The nearly uniform tropical warming seen in the leading pattern, and the Southern Hemisphere

TABLE 4. Correlation between the SST PC associated with rotated EOF mode *n* and the time series associated with optimal pattern *n* of 200-hPa height for each of the three GCMs. Numbers in boldface are significant at the 99% level.

Season	Mode *n*	COLA	NSIPP	NCEP
SON	1	**0.72**	**0.74**	0.47
SON	2	**0.71**	**0.83**	**0.65**
JFM	1	**0.91**	**0.92**	**0.95**
MAM	1	**0.94**	**0.97**	**0.96**

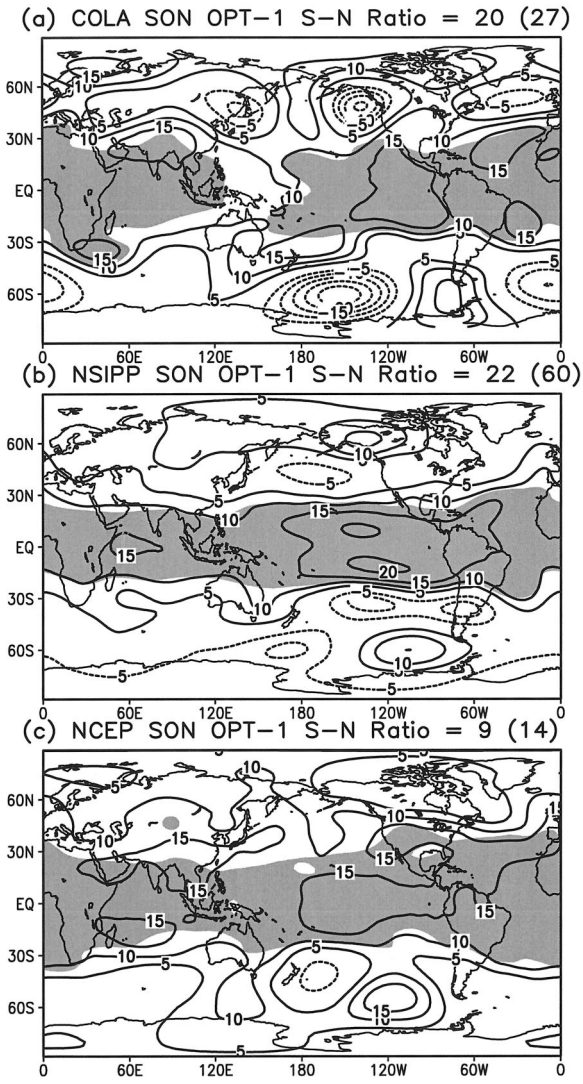

FIG. 14. As in Fig. 12, but for boreal autumn. Note that the contour interval is 5 m.

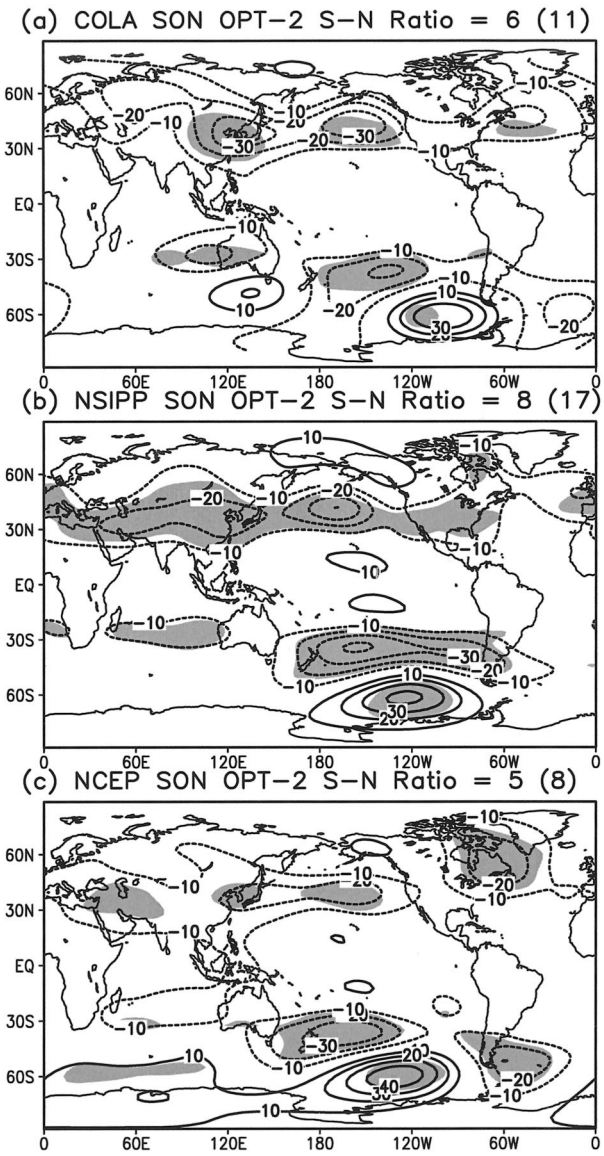

FIG. 15. As in Fig. 12, but for the second optimal pattern during boreal autumn.

wave trains and Northern Hemisphere lows seen in the Pacific, Asia, and even over the Atlantic in the second optimal pattern, are all seen in the corresponding regression results of S2. However, the zonally symmetric nature of the summer response in S2 is less evident in the autumn optimal patterns.

8. Summary and conclusions

The characteristics of the seasonal-mean response forced by global SST boundary conditions are difficult to estimate directly from observations because of the large noise component arising from nonlinear, chaotic dynamics. The use of ensembles of GCM simulations allows us in principle to obtain separate estimates of the true boundary-forced signal and the noise. This becomes particularly important during the transition seasons when the signal is smaller than in winter. In this study we have extended the Dynamical Seasonal Prediction project (Shukla et al. 2000a) by focusing on the transition seasons. We have, in particular, examined the forced response, the noise variance, and their model dependence utilizing ensemble seasonal simulations from three GCMs. The optimal signal-to-noise patterns, used here for the first time to compare GCM results, make use of the entire probability distribution of the ensemble, not just the ensemble mean.

The signal and noise variances of the GCMs for seasonal-mean 200-hPa heights are generally similar to each other and do not display the striking differences seen in earlier studies (e.g., Shukla et al. 2000a). The warm-minus-cold composite precipitation and height

fields for the boreal springs following the large winter events show patterns generally similar to those for winter, both in the ensemble mean GCM results and in observations. In particular, the equatorial eastern Pacific precipitation anomalies have similar magnitudes in winter and spring. However, the composites using the boreal autumns preceding the large winter events show much weaker global height responses, and an equatorial precipitation signal that is much weaker in the eastern Pacific, corresponding to the complete absence of water warm enough to excite convection. These findings suggest that the winter ENSO response paradigm of a wave train extending from the subtropical Pacific to North America is more applicable to boreal spring than to boreal autumn.

This suggestion is strengthened by a fuller analysis of both the tropical SST patterns and the global height response. The interannual variation of the pattern that has the largest signal-to-noise ratio for 200-hPa height is highly correlated with the PC time series of the leading SST REOF pattern for both boreal spring and winter, and for all three GCMs. These results suggest that, to leading order, the signal defined from optimal analysis is in fact linear in SST.

In this context it is worth remembering that the midlatitude seasonal-mean response to tropical SST forcing depends not only on the associated tropical precipitation anomalies but equally importantly on the climatological mean flow (Peng et al. 1997) and the feedback of the anomalous midlatitude transient fluxes of sensible heat and vorticity (Held et al. 1989). Differences between GCMs' simulations of the mean flow and transients and those observed are therefore very relevant to understanding the simulated response to tropical SSTs.

The similarity between boreal spring and winter responses may be due in part to the fact that the month of March is common to the two seasons as we have defined them. A more traditional choice of winter as the period of December–February would have eliminated this problem, without, we believe, substantially changing the results.

During boreal autumn, two modes of SST variability and two global height signals emerge. The eastern tropical Pacific SST variability excites a general (weak) tropical warming, but cannot excite well-defined wave trains as in the other seasons because of the lack of warm water in the eastern Pacific even during warm events. The SST pattern that strongly weights the central equatorial Pacific is correlated at about the 0.70 level with a height response showing both an intense wave train in the Southern Hemisphere and more modest and more zonally symmetric features in the Northern Hemisphere. Strong similarities with the summer season behavior found by S2 were noted.

The ensemble simulations of the three GCMs utilized agree reasonably well with each other in terms of the overall level of signal and noise, and on the forced signals and their relationship to the dominant SST patterns in boreal spring and autumn. Spring appears much closer to winter, with the dominant signal related to the eastern tropical Pacific warm SST events via enhanced tropical convection there. The relatively weak midlatitude signals in autumn, on the other hand, appear more closely related to warming and enhanced convection in the central Pacific.

Based on the agreement between the optimal mode analysis and the linear regression of the height field on the leading SST modes (which are heavily weighted in the tropical Pacific), we conclude that the dominant forced signals are closely related to tropical *Pacific* forcing. Yet we cannot preclude the possibility that tropical *Atlantic* forcing can also produce a discernible response that appears above the chaotic noise level. Since such a signal appears to be relatively weak compared to the Pacific response, its study would require GCM simulations in which the specified SST varies from year to year only in the Atlantic.

A caveat in this study relates to an important similarity of the three GCMs. All three GCMs use very similar versions of the relaxed Arakawa–Schubert convection parameterization. Since this parameterization is centrally involved in converting the SST anomaly provided as a boundary condition into a deep tropical convective heat source, its behavior may have a strong effect on the simulation of the forced response. Further GCM comparisons, encompassing a wider suite of model parameterizations, are needed.

The success of the approach used provides a framework for posing further dynamical questions related to the transition season signals. For example, what are the roles of the transients and of the propagation characteristics of the mean three-dimensional circulation in modulating the tropical forced signals? How important are intraseasonal variations in SST in altering the signals?

Acknowledgments. We are indebted to Dr. T. DelSole for introducing us to the optimal pattern technique, and for providing us with the relevant computer programs. This work was supported by the National Science Foundation under Grant ATM-98-14295, the National Aeronautics and Space Administration (NASA) under Grant NAG5-8 208, and the National Oceanic and Atmospheric Administration (NOAA) under Grant NA96-GP0056. We also wish to gratefully acknowledge the support of the NASA Seasonal to Interannual Prediction Project, and of NOAA's Climate Diagnostics and Experimental Prediction Program.

APPENDIX

Optimizing Signal to Noise

a. Theory

Denoting the variable X at grid point i, time n, where $1 \leq n \leq N$, and for ensemble member m, where $1 \leq$

$m \leq M$, as X_{inm}, we consider an expansion of X in terms of a set of patterns P and their associated time series α:

$$X_{inm} = \sum_r P_i^r \alpha_{nm}^r, \tag{A1}$$

where the index r denotes the mode, or pattern. The only prior constraint we place on this expansion is that the time series α be derivable from a linear transformation of the original data:

$$\alpha_{nm}^r = \sum_i e_i^r X_{inm}. \tag{A2}$$

Define the ensemble average with an overbar,

$$\overline{A}_n = \frac{1}{M} \sum_m A_{nm}, \tag{A3}$$

and the time average with square brackets:

$$[A]_m = \frac{1}{N} \sum_n A_{nm}. \tag{A4}$$

Assuming that the climate (ensemble time mean) has been removed, so that

$$[\overline{X_{inm}}] = 0 \tag{A5}$$

for all i, we also then have

$$[\overline{\alpha_{nm}^r}] = [\overline{\alpha}_n^r] = 0. \tag{A6}$$

The *signal* S and *noise* N are defined in terms of the time series of a particular mode, or pattern:

$$\mathcal{S} = [(\overline{\alpha}_n^r)^2] \quad \text{and} \tag{A7}$$

$$\mathcal{N} = [\overline{(\alpha_{nm}^r - \overline{\alpha}_n^r)^2}]. \tag{A8}$$

Temporarily omitting the pattern index r, and considering the rth column of e_i^r to be a vector e_i, we can write

$$\mathcal{S} = \left[\left(\sum_i e_i \overline{X}_{in}\right)^2\right] = \left[\left(\sum_i e_i \overline{X}_{in} \sum_j e_j \overline{X}_{jn}\right)\right] = \sum_i \sum_j e_i([\overline{X}_{in}\overline{X}_{jn}])e_j. \tag{A9}$$

Defining

$$A_{ij} = [\overline{X}_{in}\overline{X}_{jn}] \tag{A10}$$

as the (square symmetric and positive definite) covariance matrix of the ensemble means, the signal becomes

$$\mathbf{S} = \sum_i e_i A_{ij} e_j = \mathbf{e}^{\mathrm{T}} \cdot \mathbf{A} \cdot \mathbf{e}, \tag{A11}$$

where lowercase (uppercase) boldface letters are used to refer to vectors (matrices) and the superscript T denotes the matrix transpose.

In a similar way, using (A2), the noise can be written as

$$\mathcal{N}\left[\left(\sum_i e_i (X_{inm} - \overline{X}_{in})\right)^2\right] = \frac{1}{N} \sum_n \overline{\left(\sum_i e_i X'_{inm}\right)^2}, \tag{A12}$$

where we have defined the primes to denote the noise, that is, the deviations about the ensemble mean:

$$X'_{inm} = X_{inm} - \overline{X}_{in}. \tag{A13}$$

There is a relationship giving the time series of the noise in terms of the original data, derived from (A2) by subtracting the ensemble mean:

$$\alpha'^r_{nm} = \sum_i e_i^r X'_{inm}. \tag{A14}$$

Similar to the development following (A9) we can write the noise as

$$\mathcal{N} = \sum_i e_i B_{ij} e_j = \mathbf{e}^{\mathrm{T}} \cdot \mathbf{B} \cdot \mathbf{e}, \tag{A15}$$

where B_{ij} is the square symmetric and positive definite covariance matrix of deviations about the ensemble mean:

$$B_{ij} = [\overline{X'_{inm} X'_{jnm}}]. \tag{A16}$$

Now the signal-to-noise ratio $\mathcal{R} = \mathcal{S}/\mathcal{N}$ is just

$$\mathcal{R} = \frac{\mathbf{e}^{\mathrm{T}} \cdot \mathbf{A} \cdot \mathbf{e}}{\mathbf{e}^{\mathrm{T}} \cdot \mathbf{B} \cdot \mathbf{e}}. \tag{A17}$$

The denominator can be diagonalized utilizing the vector $\mathbf{g}$, which is defined as

$$\mathbf{g} = \mathbf{B}^{1/2} \cdot \mathbf{e} \quad \text{or} \tag{A18}$$

$$\mathbf{e} = \mathbf{B}^{-1/2} \cdot \mathbf{g}. \tag{A19}$$

Note that the matrix $\mathbf{B}^{1/2}$ and its inverse are also square symmetric (and positive definite) matrices. Using (A19), it is straightforward to show that the ratio $\mathcal{R}$ can be written as

$$\mathcal{R} = \frac{\mathbf{g}^{\mathrm{T}} \cdot \mathbf{C} \cdot \mathbf{g}}{\mathbf{g}^{\mathrm{T}} \cdot \mathbf{g}}, \tag{A20}$$

where the (square symmetric and positive definite) matrix $\mathbf{C}$ is defined as

$$\mathbf{C} = (\mathbf{B}^{-1/2})^{\mathrm{T}} \cdot \mathbf{A} \cdot \mathbf{B}^{-1/2}. \tag{A21}$$

Equation (A20) is of Rayleigh quotient form. By the Rayleigh quotient theorem, the maximum value of $\mathcal{R}$ is the maximum eigenvalue of $\mathbf{C}$, and this maximum is obtained when $\mathbf{g}$ equals the corresponding eigenvector. The eigenvectors are orthogonal:

$$(\mathbf{g}^r)^{\mathrm{T}} \cdot \mathbf{g}^s = \delta_{r,s}, \tag{A22}$$

which becomes, using (A18),

$$(\mathbf{e}^r)^{\mathrm{T}} \cdot \mathbf{B} \cdot \mathbf{e}^s = \delta_{r,s}. \tag{A23}$$

In these equations r and s refer to modes in the eigenvector expansion. This can be further written, using (A16), as

$$\sum_i \sum_j e_i^r B_{ij} e_j^s = \sum_i \sum_j e_i^r [\overline{X'_{inm} X'_{jnm}}] e_j^s = [\overline{\alpha'^r_{nm} \alpha'^s_{nm}}] = \delta_{r,s}, \tag{A24}$$

where we have used (A14).

The set of modes derived from this eigenvalue/eigenvector problem are identified as the modes that optimize the signal-to-noise ratio R. Through (A19), (A1), (A2), and (A14), these modes define the optimal patterns $\mathbf{P}^r$ and the corresponding time series for the signal and noise ($\overline{\alpha}^r_n$ and α'^r_{nm}). Note that the patterns $\mathbf{P}^r$ are called the *physical* patterns, and the patterns $\mathbf{e}^r$ used to derive the time series are called the *filter* patterns. From (A24) we see that the noise time series corresponding to different modes are independent.

The physical pattern P_i^r can be obtained directly by writing the version of (A1) for the noise:

$$X'_{inm} = \sum_r P_i^r \alpha'^r_{nm}. \tag{A25}$$

Multiplying this equation by α'^s_{nm}, averaging over time and ensemble members, and using (A24) we obtain

$$[\overline{\alpha'^s_{nm} X'_{inm}}] = \sum_r P_i^r [\overline{\alpha'^s_{nm} \alpha'^r_{nm}}] = P_i^s. \tag{A26}$$

But from (A14) for mode s,

$$\alpha'^s_{nm} = \sum_j e_j^s X'_{jnm}, \tag{A27}$$

so that

$$P_i^s = \sum_j e_j^s [\overline{X'_{jnm} X'_{inm}}] = \sum_j e_j^s B_{ij}. \tag{A28}$$

When multiplied by e_i^r and summed over i, this gives [using (A24)]

$$\sum_i e_i^r P_i^s = \delta_{r,s}, \tag{A29}$$

showing that the physical and filter patterns form a biorthogonal set.

b. Calculation and signficance tests

In practice, the fields X_{inm} are represented in terms of an EOF expansion to carry out these calculations. We performed calculations using both 10 and 20 EOFs. The leading two optimal patterns were nearly identical in all cases, although there is some small difference in the signal-to-noise ratio. The ratios shown in Figs. 12–15 are for the 10-EOF truncation; those ratios in parentheses are for the 20-EOF calculation. The difference between them is much less than the difference in the ratios between GCMs.

Ths confidence interval for the signal to noise ratio was estimated by using a random sampling approach, starting with an expanded ensemble of 55 simulations of the COLA GCM for each of the 18 winters used in the paper. (The JFM COLA ensembles used earlier in the paper formed a subset of this larger set.) The calculation of signal-to-noise optimal patterns and ratios was carried out for randomly chosen sets of ensemble size 10 using all 18 yr. This procedure was repeated 200 times. The 200-sample average signal-to-noise ratios for the leading two optimals were 60.9 and 10.9, with a corresponding standard deviation of 8.4 and 1.4, respectively. This gives an effective confidence interval of about ±13% to 14% for the ratio. While these estimates apply only for the COLA GCM in boreal winter, they provide some assurance that the confidence levels are fairly narrow.

In order to assess what regions of the optimal patterns are ''significant,'' we proceeded as follows: We take the ensemble mean of (A1) to obtain an expansion of the ensemble mean fields in terms of optimal modes, and compute the temporal variance of the field obtained by keeping either the leading $r = 1$ or $r = 2$ mode. The ratio of either of these variances to the total temporal variance of the ensemble means gives a measure of the ensemble mean variance ''explained'' by the optimal mode. The shading in Figs. 12–15 corresponds to values of this ratio that exceed 0.50.

REFERENCES

Bacmeister, J. T., and M. J. Suarez, 2002: Wind stress simulations and the equatorial momentum budget in an AGCM. *J. Atmos. Sci.*, **59,** 3051–3073.

Bates, G. T., M. P. Hoerling, and A. Kumar, 2001: Central U. S. springtime precipitation extremes: Teleconnections and relationships with sea surface temperature. *J. Climate,* **14,** 3751–3766.

Branković, C., and T. N. Palmer, 1997: Atmospheric seasonal predictability and estimates of ensemble size. *Mon. Wea. Rev.*, **125,** 859–874.

——, and ——, 2000: Seasonal skill and predictability of ECMWF PROVOST ensembles. *Quart. J. Roy. Meteor. Soc.*, **126,** 2035–2067.

Chang, Y., S. D. Schubert, and M. J. Suarez, 2000: Boreal winter predictions with the GEOS-2 GCM: The role of boundary forcing and initial conditions. *Quart. J. Roy. Meteor. Soc.*, **126,** 2293–2323.

Held, I. M., S. W. Lyons, and S. Nigam, 1989: Transients and the extratropical response to El Niño. *J. Atmos. Sci.*, **46,** 163–174.

Hoerling, M. P., M. Ting, and A. Kumar, 1995: Zonal flow–stationary wave relationship during El Niño: Implications for seasonal forecasting. *J. Climate,* **8,** 1838–1852.

——, A. Kumar, and T. Xu, 2001: Robustness of the nonlinear climate response to ENSO's extreme phases. *J. Climate,* **14,** 1277–1293.

Kalnay, E., and Coauthors, 1996: The NCEP/NCAR 40-Year Reanalysis Project. *Bull. Amer. Meteor. Soc.*, **77,** 437–471.

Kanamitsu, M., and Coauthors, 2002: NCEP dynamical seasonal forecast system 2000. *Bull. Amer. Meteor. Soc.*, **83,** 1019–1037.

Kiehl, J. T., J. J. Hack, G. Bonan, B. A. Boville, D. L. Williamson, and P. J. Rasch, 1998: The National Center for Atmospheric Research Community Climate Model: CCM3. *J. Climate,* **11,** 1131–1149.

Koster, R. D., and M. J. Suarez, 1992: A comparative analysis of two land surface heterogeneity representations. *J. Climate,* **5,** 1379–1390.

Kumar, A., and M. P. Hoerling, 1998: Annual cycle of Pacific–North American seasonal predictability associated with different phases of ENSO. *J. Climate,* **11,** 3295–3308.

——, A. G. Barnston, P. Peng, M. P. Hoerling, and L. Goddard, 2000: Changes in the spread of the variability of the seasonal mean

atmospheric states associated with ENSO. *J. Climate,* **13,** 3139–3151.

Livezey, R. E., M. Masutani, A. Leetmaa, H. Rui, M. Ji, and A. Kumar, 1997: Teleconnective response of the Pacific–North American region atmosphere to large central equatorial Pacific SST anomalies. *J. Climate,* **10,** 1787–1820.

Moorthi, S., and M. J. Suarez, 1992: Relaxed Arakawa–Schubert: A parameterization of moist convection for general circulation models. *Mon. Wea. Rev.,* **120,** 978–1002.

Pan, H.-L., and L. Mahrt, 1987: Interaction between soil hydrology and boundary layer developments. *Bound.-Layer Meteor.,* **38,** 185–202.

Peng, S., W. A. Robinson, and M. P. Hoerling, 1997: The modeled atmospheric response to midlatitude SST anomalies and its dependence on background circulation states. *J. Climate,* **10,** 971–987.

Reynolds, R. W., and T. M. Smith, 1994: Improved global sea surface temperature analyses using optimal interpolation. *J. Climate,* **7,** 929–948.

Rowell, D. P., C. K. Folland, K. Maskell, and M. N. Ward, 1995: Variability in summer rainfall over tropical North Africa (1906–92): Observations and modelling. *Quart. J. Roy. Meteor. Soc.,* **121,** 669–704.

Scheffé, H., 1959: *The Analysis of Variance.* John Wiley and Sons, 477 pp.

Schneider, E. K., 2002: Understanding differences between the equatorial Pacific as simulated by two coupled GCMs. *J. Climate,* **15,** 449–469.

Schubert, S. D., M. J. Suarez, Y. Chang, and G. Branstator, 2001: The impact of ENSO on extratropical low-frequency noise in seasonal forecasts. *J. Climate,* **14,** 2351–2365.

——, ——, P. J. Pegion, M. A. Kistler, and A. Kumar, 2002: Predictability of zonal means during boreal summer. *J. Climate,* **15,** 420–434.

Shukla, J., and Coauthors, 2000a: Dynamical seasonal prediction. *Bull. Amer. Meteor. Soc.,* **81,** 2593–2606.

——, D. A. Paolino, D. M. Straus, D. DeWitt, M. Fennessy, J. L. Kinter, L. Marx, and R. Mo, 2000b: Dynamical seasonal prediction with the COLA atmospheric model. *Quart. J. Roy. Meteor. Soc.,* **126,** 2265–2291.

Smith, T. M., R. W. Reynolds, R. E. Livezey, and D. C. Stokes, 1996: Reconstruction of historical sea surface temperatures using empirical orthogonal functions. *J. Climate,* **9,** 1403–1420.

Straus, D. M., and J. Shukla, 2000: Distinguishing between the SST-forced variability and internal variability in mid latitudes: Analysis of observations and GCM simulations. *Quart. J. Roy. Meteor. Soc.,* **126,** 2323–2350.

——, and ——, 2002: Does ENSO force the PNA? *J. Climate,* **15,** 2340–2358.

Suarez, M. J., and L. L. Takacs, 1995: Documentation of the Aires/GEOS dynamical core version 2. NASA Tech. Memo 104606, Vol. 10, 56 pp.

Venzke, S., M. R. Allen, R. T. Sutton, and D. P. Rowell, 1999: The atmospheric response over the North Atlantic to decadal changes in sea surface temperature. *J. Climate,* **12,** 2562–2584.

Xie, P., and P. A. Arkin, 1997: Global precipitation: A 17-year monthly analysis based on gauge observations, satellite estimates, and numerical model outputs. *Bull. Amer. Meteor. Soc.,* **78,** 2359–2558.

Xue, Y.-K., P. J. Sellers, J. L. Kinter, and J. Shukla, 1991: A simplified biosphere model for global climate studies. *J. Climate,* **4,** 345–364.